Biosensors and Bioelectronics 171 (2021) 112736

Contents lists available at ScienceDirect

Biosensors and Bioelectronics

journal homepage: http://www.elsevier.com/locate/bios

High-performance field-effect transistor glucose biosensors based on bimetallic Ni/Cu metal-organic frameworks

Bingfang Wang [a,b], Yuanyuan Luo [b,c], Lei Gao [b,c], Bo Liu [a], Guotao Duan [a,*]

[a] Wuhan National Laboratory for Optoelectronics, School of Optical and Electronic Information, Huazhong University of Science and Technology, Wuhan, 430074, China
[b] Key Lab of Materials Physics, Anhui Key Lab of Nanomaterials and Nanotechnology, Institute of Solid State Physics, Chinese Academy of Sciences, Hefei, 230031, China
[c] University of Science and Technology of China, Hefei, 230026, China

ARTICLE INFO

Keywords:
Bimetallic metal-organic framework
Glucose detection
Biosensor
Field effect transistor
In situ growth method

ABSTRACT

Accurate detection of glucose is essential for the diagnosis of diabetes, wherein effective and sensitive biosensors for glucose detection are needed. Here, we fabricated a glucose sensor based on field-effect transistor (FET) with bimetallic nickel-copper metal-organic frameworks (Ni/Cu-MOFs) as its channel layers which were grown *in-situ* through a simple one-step hydrothermal method and modified with glucose oxidase (GOD) by using glutaraldehyde (GA) as linkers. Due to the synergistic effect of Ni ions and Cu ions in MOFs, the sensor (GOD-GA-Ni/Cu-MOFs-FET) showed good field effect performance and great responses to glucose through enzymatic reactions. It displayed a piecewise linear relationship in the wide range (1 μM–20 mM), and provided high sensitivity (26.05 $\mu A cm^{-2} mM^{-1}$) in the low concentration (1–100 μM) and a low detection limit (0.51 μM). The sensor also had these advantages of high specificity, excellent reproducibility, good short-term stability and fast response time. Especially, it is indicated that the Ni/Cu-MOFs-FETs with high performance have the potential to be available sensors, paving the way for the application of bimetallic MOFs in biosensing.

1. Introduction

Diabetes is a chronic disease caused by insufficient insulin in the pancreas or the ineffective insulin (King et al., 1998; Colmegna et al., 2016). It poses a huge threat to human health, inducing cardiovascular, cerebrovascular, microvascular diseases and even increasing the risk of cancer (Heidari and Habibi, 2016; Li et al., 2017; Yadav et al., 2015). Diabetes is closely related to blood glucose levels, and blood glucose concentration is a key indicator for detecting diabetes (Wang, 2008; Wang and Lee, 2015). Therefore, accurate detection of glucose in the blood is of great significance for the diagnosis of diabetes. In recent decades, various techniques for glucose detection have been developed, for example, electrochemical methods (ampere method (Roda et al., 2020)), potential method (Chen et al., 2015; Kim et al., 2017), optical methods (Raman spectroscopy (Luo et al., 2019), infrared spectroscopy (Depciuch et al., 2019) and surface plasmon resonance (Vikas et al., 2020), colorimetry (Zuo et al., 2020) and mass spectrometry (Rahman et al., 2010). Among these methods, electrochemical methods have attracted considerable interest due to their simple equipment configuration, high sensitivity and reliability, low detection limits and cost effectiveness. Electrochemical glucose sensors can be divided into enzyme-based sensors and non-enzyme-based sensors (Kou et al., 2020). The detection principle of the enzyme-based glucose sensors is to utilize the enzymatic reaction between glucose oxidase and glucose, which has high sensitivity and good selectivity (Dhanjai et al., 2020; Liu et al., 2017; Piao et al., 2015).

Metal-organic frameworks (MOFs) possess many special features, such as high specific surface area, adjustable pore structure, abundant and modifiable metal sites, *etc.* (Li et al., 2020; Liao et al., 2019). These above advantages enable MOFs widely used in electrochemical catalysis, sensing and energy storage (Abuzalat et al., 2020; Wei et al., 2019; Zhou et al., 2020). In particular, MOFs can be used to detect many substances because of their high reactivity (Yang and Yang, 2020), such as Cu–H MOFs/NECF for detecting trichlorfon (Song et al., 2018), Cu-BTC doped with ball-milled graphene for detecting bisphenol A and p-chlorophenol. 2 (Chen et al., 2018), and Zr-MOFs modified with Ag nanoclusters for detecting carcinoembryonic antigen (Guo et al., 2017a). However, there are few reports on the direct use of MOFs to detect glucose. For example, metal oxide complexes prepared by calcining MOFs precursors were tested to catalyze glucose (Zhang et al., 2020), or the MOFs with porous

* Corresponding author.
E-mail address: duangt@hust.edu.cn (G. Duan).

https://doi.org/10.1016/j.bios.2020.112736
Received 2 July 2020; Received in revised form 11 October 2020; Accepted 14 October 2020
Available online 15 October 2020

structure were used to encapsulate metal nanoparticles for glucose detection (Zhu et al., 2019). Bimetallic MOFs materials have entered the research field because of their excellent properties. Bimetallic MOFs have higher reactivity than monometallic MOFs due to the introduction of different unsaturated metal ions and the synergistic effect between metal centers (Shen et al., 2017; Su et al., 2018; Zhou et al., 2019). In addition, the metal active sites of bimetallic MOFs are more abundant, which makes them own good electrical conductivity and promotes the electrons transfer within bimetallic MOFs (Fang et al., 2019; Guo et al., 2017b; Zhao et al., 2018). Therefore, bimetallic MOFs have great potential for application in chemical and biomolecular detection.

In this work, a new type of glucose biosensor (GOD-GA-Ni/Cu-MOFs-FET) based on bimetallic Ni/Cu-MOFs was prepared via a simple, one-step hydrothermal method (Fig. 1). Large and uniform Ni/Cu-MOFs films were grown *in situ* on the substrate of pre-prepared FET devices as channel layers, and modified with glucose oxidase. In order to immobilize the enzyme and improve the sensitivity of sensing, glutaraldehyde was used as a linker between glucose oxidase and MOFs. Meanwhile, the feeding molar ratios of Ni ions and Cu ions were changed from 1:7 to 1:1, 7:1, 20:1 and 30:1 to study the effect on the properties of bimetallic MOFs. The field effect performance test of the fabricated sensor and its glucose detection were conducted, and compared with monometallic Ni-MOFs. The Ni/Cu-MOFs-FET had better electrical conductivity and excellent specific response to glucose in the presence of interfering substances (sucrose, fructose, uric acid, ascorbic acid, galactose and lactose), which exhibited considerable potential for glucose detection.

2. Experiment

2.1. Materials

2,3,6,7,10,11-hexaaminohexatyl hydrogen hexachloride (HATP·6HCl) was purchased from Chemsoon Co., Ltd. (Shanghai, China). Nickel chloride hexahydrate ($NiCl_2{\cdot}6H_2O$), copper sulfate pentahydrate ($CuSO_4{\cdot}5H_2O$), absolute ethanol (EtOH), ammonium hydroxide ($NH_3{\cdot}H_2O$), acetone and glutaraldehyde (GA) were all purchased from Sinopharm Chemical Reagent Co., Ltd. (Shanghai, China). Glucose oxidase (GOD) was purchased from Sigma-Aldrich (St. Louis, USA). Bovine serum albumin (BSA), glucose, sucrose, fructose, uric acid (UA), ascorbic acid (AA), galactose, lactose and phosphate buffer saline (PBS, pH = 7.4) were purchased from Aladdin (Shanghai, China). All chemicals were used without further purification. Deionized water was used in this experiment.

2.2. Fabrication of Ni/Cu-MOFs-FET

The FET device was prepared according to the steps in S1(Supplementary Information (SI)). 6.6 g $NiCl_2.6H_2O$ (0.028 mmol) and 1.0 g $CuSO_4.5H_2O$ (0.004 mmol) were dissolved in 5 mL deionized water to obtain a mixed solution of nickel metal ions and copper metal ions with a molar ratio of 7:1, and then 0.3 mL $NH_3{\cdot}H_2O$ was added dropwise under stirring. 10.0 mg HATP·6HCl (0.028 mmol) was dissolved in 5 mL deionized water, and the prepared solution with mixed metal ions was slowly added into the ligand solution. The subsequent steps were the same as those for preparing Cu-MOFs-FET (SI), and the Ni/Cu-MOFs (7:1) -FET was obtained. In addition, bimetallic Ni/Cu-MOFs with different feeding molar ratios of 1:7, 1:1, 10:1, 20:1 and 30:1 were prepared, and labeled as Ni/Cu-MOFs (1:7)-FET, Ni/Cu-MOFs (1:1)-FET, Ni/Cu-MOFs (10:1)-FET, Ni/Cu-MOFs (20:1)-FET and Ni/Cu-MOFs (30:1)-FET respectively.

2.3. Modification of glucose sensor (GOD-GA-Ni-MOFs (7:1)-FET)

Firstly, 1.0 mg/mL GOD solution was prepared with PBS solution, and GA was diluted with PBS solution to a concentration of 0.25%. Then, 5 μL of diluted GA was pipetted into the liquid cell of the Ni/Cu-MOFs (7:1)-FET device, which was incubated at room temperature for 60 min and was rinsed with PBS solution several times to remove the residual GA. Next, 5 μL GOD solution was added dropwise to the liquid cell of the FET device, which was placed in a refrigerator and incubated overnight at 4 °C. After incubation, the FET was rinsed with a small amount of PBS solution several times to remove the residual GOD. After drying at room temperature for 5–10 min, the sensor (GOD-GA-Ni/Cu-MOFs (7:1)-FET) was obtained for glucose test. For comparison, GOD-GA-Ni-MOFs (7:1)-FET using monometallic Ni-MOFs modified with GA and GOD, and GA-Ni/Cu-MOFs (7:1)-FET only modified with GA without GOD were prepared. In addition, GOD-GA-Ni/Cu-MOFs (7:1)-FET was blocked with 5 μL BSA (1 wt%) for 12 h at 4 °C and marked as BSA-GOD-GA-Ni/Cu-MOFs (7:1)-FET.

2.4. Characterization of morphology and structure

The scanning electron microscope (SEM, Hitachi SU8020, Japan) and transmission electron microscope (TEM, JEM, 2010, Japan) were used to observe the surface morphology and cross-sectional thickness of the MOFs thin film. Atomic force microscope (AFM, Park System NX-HDM, Korea) was used to analyze the roughness of materials. Powder X-ray diffraction (PXRD, Philips X′ Pert, Japan), X-ray photoelectron spectroscopy (XPS, Thermo Fisher Scientific ESCALAB 250, England), Fourier transform infrared (FTIR, Thermo Nicolet Corporation NEXUS, USA), contact angle instrument (Shanghai Solon Tech. Co., Ltd SL 200B, China), inductively coupled plasma mass spectrometry (ICP-MS, Perkin-Elmer nexION 1000G, USA) and thermogravimetry analysis (TGA, Perkin-Elmer SDT Q600, USA, in air atmosphere at a rate of 10 °C·min^{-1}) were used to further study the structure and properties of Ni/Cu-MOFs prepared by the *in situ* growth method.

2.5. Device's electrical performance

The electrical performances of Ni/Cu-MOFs (7:1)-FET, GOD-GA-Ni/Cu-MOFs (7:1)-FET and Cu-MOFs-FET as liquid-gated devices were measured by using 4200 semiconductor parameter analyzer and four-point probe station (Keithley 4200-SCS, USA). First, 5 μM PBS solution

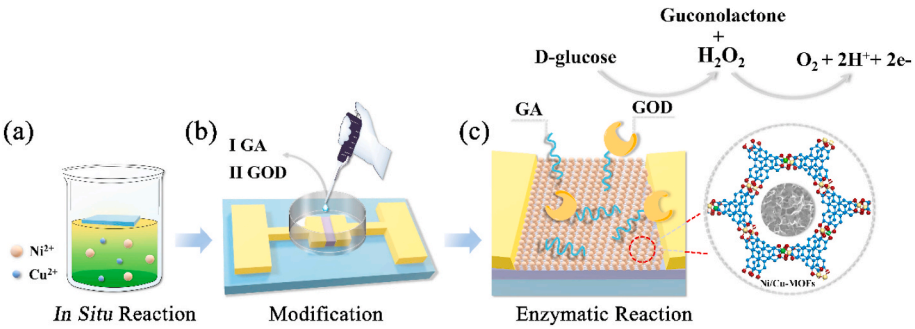

Fig. 1. Schematic diagram of the fabrication, modification and the principle of the glucose detection of the GOD-GA-Ni/Cu-MOFs-FET. (a) The FET was suspended on the surface of reaction solution with mixed metal ions. Insert showed the respond time of the sensor to glucose. (b) The Ni/Cu-MOFs was modified by dropping GA and GOD sequentially for cultivation. (c) Ions generated from the enzymatic reaction of glucose accumulated on the surface of bimetallic MOFs films, inducing the change of charges concentration.

was dropped into the liquid cell of the FET, and the silver probe was placed vertically in the PBS solution to serve as a gate electrode. The output characteristic curve (I_{ds}-V_{ds}) of the device was obtained when the gate voltage (V_{gs}) was changed from 0.1 V to −0.1 V in the step of −0.1 V and the source-drain voltage (V_{ds}) was set in the range of 0 ~ −0.2 V. In addition, the transfer characteristic curve (I_{ds}-V_{gs}) was obtained when the V_{ds} was fixed at −0.10 V and the V_{gs} was set in the range of −0.15–0.15 V.

2.6. Device's glucose detection capabilities

pH test: PBS solutions with various pH values of 5.8, 6.4, 6.8, 7.4 and 8 were made by mixing a 2 mM NaH_2PO_4 solution and a 2 mM Na_2HPO_4 solution. When V_g was set to −0.1 V, 5 μL PBS solutions of different pHs were added dropwise in sequence to the liquid cell of the GOD-GA-Ni/Cu-MOFs (7:1)-FET, and then the I-V_{ds} curves were tested three times at each pH.

Concentration test: the current that changed with glucose concentration within a period of time (300 s) was measured when the V_{gs} and the V_{ds} were both fixed at −0.10 V. First, 5 μL PBS solution was pipetted into the liquid cell of the FET device and tested as a blank sample. Next, 5 μL glucose solutions of different concentrations (1 μM–50 mM) were added respectively from low to high concentration. In order to eliminate interference, the device was rinsed with PBS solution three times before the next concentration test. The concentration tests of GOD-GA-Ni/Cu-MOFs (7:1)-FET, GOD-GA-Ni-MOFs-FET, GA-Ni/Cu-MOFs (7:1)-FET and Ni/Cu-MOFs (7:1)-FET were conducted respectively according to the above steps.

Specificity, reproducibility and stability test: sucrose, fructose, UA, AA, galactose and lactose were used as interferences to explore the specificity of the GOD-GA-Ni/Cu-MOFs (7:1)-FET for glucose detection. The current changes of the sensor were tested when 5 μL glucose of 100 μM and interfering substances were added in sequence. Glucose concentration tests of three GOD-GA-Ni/Cu-MOFs (7:1)-FET devices were conducted under the same condition to study the reproducibility. In order to evaluate the stability, one GOD-GA-Ni/Cu-MOFs (7:1)-FET was placed under constant temperature and humidity conditions for a week, and its glucose detection performance was tested every two days in a week.

3. Discussion

3.1. Morphology and structure

The PXRD patterns of Ni-MOFs films, Cu-MOFs films and Ni/Cu-MOFs (7:1) films were shown in Fig. 2a. The diffraction peaks positions of bimetallic Ni/Cu-MOFs (7:1) were very consistent with those of monometallic MOFs whose peaks were located at 2θ = 4.7°, 9.5°, 12.5°, 16.5° and 27.1° (Sheberla et al., 2014), which indicated that Ni/Cu-MOFs (7:1) and Ni-MOFs, Cu-MOFs had similar crystal structures. The diffraction peaks at 4.7°, 9.5° and 27.1° were ascribed to the (100), (200) and (001) crystal plane of MOFs respectively. The FTIR spectra (Fig. 2b) of Ni-MOFs powders, Cu-MOFs powders and Ni/Cu-MOFs (7:1) powders further proved their similar structures with each other. The peaks at 3433 cm^{-1} were mainly ascribed to the amino groups (NH_2) of the benzene ring structure, and the characteristic peaks at 2916 cm^{-1}, 2848 cm^{-1} and 1399 cm^{-1} were derived from the out-of-plane and in-plane bending of the hydrocarbon bonds (CH) on the benzene ring. The vibration of the skeletons on the benzene ring (C═C) had a peak at 1630 cm^{-1}, and the vibration of carbon-nitrogen bonds formed between amino groups and benzene rings (C–N) showed a broad large peak at around 1109 cm^{-1} (Campbell et al., 2015). The element states of the Ni/Cu-MOFs (7:1), Ni-MOFs and Cu-MOFs were observed from the XPS spectra (Fig. 2c). In the XPS spectrum of Ni/Cu-MOFs (7:1), the binding energy peaks corresponding to O 1s, N 1s and C 1s were located at 532.43 eV, 399.00 eV and 284.94 eV respectively, and the peaks of Ni 2p (855.51 eV, 871.98 eV) and Cu 2p (934.53 eV) could be also found, which proved that both Ni ions and Cu ions participated in the

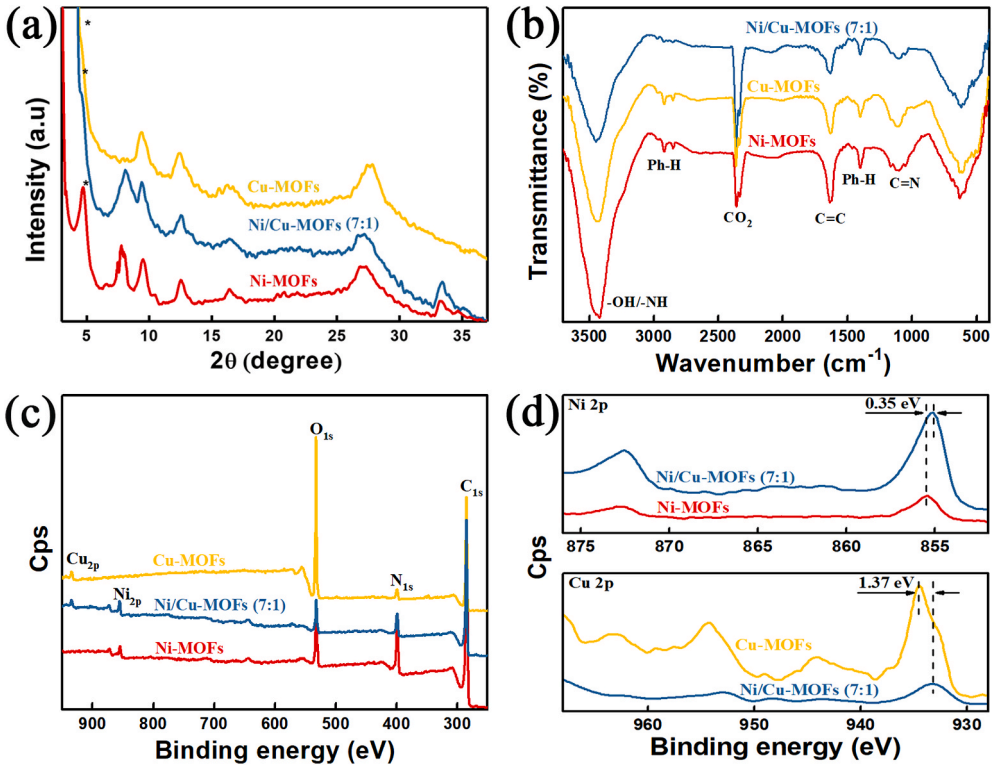

Fig. 2. (a) PXRD spectra, (b) FTIR spectra and (c) XPS spectra of Ni-MOFs, Cu-MOFs and Ni/Cu-MOFs (7:1). (d) High resolution XPS spectra of Ni 2p in Cu-MOFs and Ni/Cu-MOFs (7:1) (top), and Cu 2p in Ni-MOFs and Ni/Cu-MOFs (7:1) (bottom).

coordination with ligands to form bimetallic MOFs. In addition, in the Ni 2p spectrum (Fig. 2d), the binding energy of Ni 2p of Ni/Cu-MOFs (7:1) increased by 0.35 eV compared with that of Ni-MOFs. However, in the Cu 2p spectrum (Fig. 2d), the binding energy peak of Cu 2p of Ni/Cu-MOFs (7:1) shifted 1.37 eV towards the low binding energy direction compared with that of Cu-MOFs. The result unraveled that the local electron transfer between Ni ions and Cu ions occurred through the aromatic ring structure of the HATP ligand, which led to the Ni–Cu coupling effect. Ni ions and Cu ions could influence each other's ionic state through the benzene ring structure in the ligand, and the charge transfer between Ni and Cu was enhanced, thereby improving the overall electrical conductivity of bimetallic MOFs (Zhao et al., 2018; Cao et al., 2019). And the stronger electron acceptability of Cu ions than Ni ions made the entire electron cloud density of Ni/Cu-MOFs (7:1) tend to Cu ions, which caused a decrease in the binding energy value of Cu 2p and an increase in the binding energy value of Ni 2p. And the high resolution XPS spectra of other elements (C 1s, N 1s, O 1s) in Ni-MOFs, Cu-MOFs and Ni/Cu-MOFs (7:1) were presented in Fig. S1.

The SEM image (Fig. 3c) showed that complete and large-area Ni/Cu-MOFs (7:1) films were obtained, which had more sheet-like fold structures (Fig. 3e), and exposed more dense and tiny contact sites than Ni-MOFs films and Cu-MOFs films (Fig. 3a and b), which could increase the specific surface area of Ni/Cu-MOFs (7:1) and were more conducive to the post-modification of the surface. The cross-sectional morphology (Fig. 3h) of Ni/Cu-MOFs (7:1) indicated that the thickness of the films was about 489 nm, which was not much different from that of Ni-MOFs films (516 nm). And it could be seen that the sheet structure of Ni/Cu-MOFs (7:1) was rougher and had more tiny protrusions. The change of roughness was further proved by AFM (Fig. S2), which showed that Ni/Cu-MOFs (7:1) had greater average surface roughness of 48.27 nm than that of Ni-MOFs (28.55 nm). Surface roughness was conducive to the improvement of hydrophilicity, which was verified by the contact angle

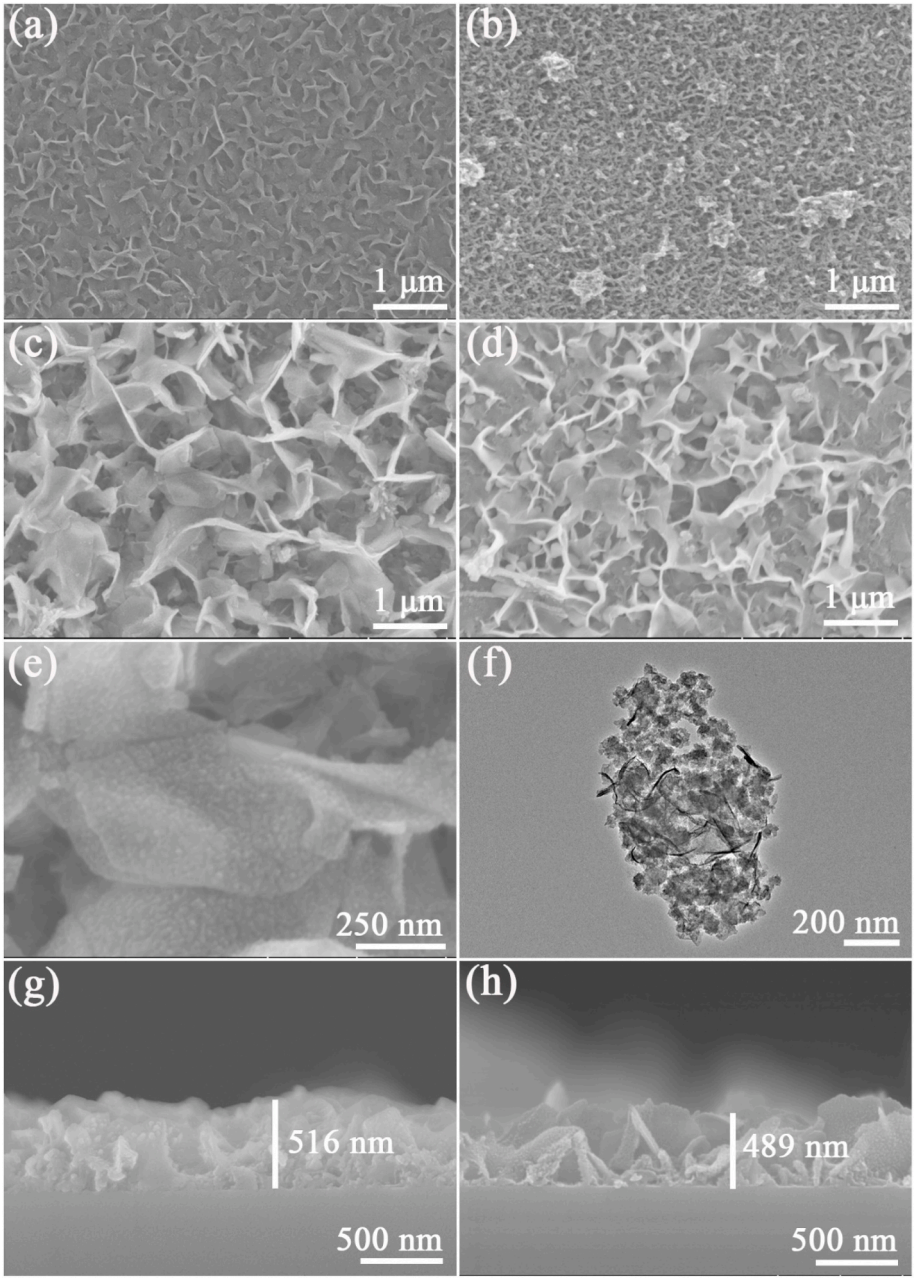

Fig. 3. SEM images of (a) Ni-MOFs; (b) Cu-MOFs; (c) Ni/Cu-MOFs (7:1); (d) GA-Ni/Cu-MOFs (7:1). (e) High resolution SEM image of Ni/Cu-MOFs (7:1). (f) TEM image of Ni/Cu-MOFs (7:1). Cross-section images of (g) Ni-MOFs and (h) Ni/Cu-MOFs (7:1).

test (Figs. S3a and b). The contact angle (101.69°) of Ni/Cu-MOFs (7:1) was smaller than that (132.20°) of Ni-MOFs, indicating that the hydrophilic property of Ni/Cu-MOFs (7:1) was improved to some extent. The morphology of GA-Ni/Cu-MOFs (7:1) was not significantly different from that of the unmodified one (Fig. 3d). However, the contact angle of GA-Ni/Cu-MOFs (7:1) decreased immensely to 52.44° (Fig. S3c), which was due to the introduction of GA with aldehyde groups making a great improvement of hydrophilic properties of GA-Ni/Cu-MOFs (7:1). The TEM image (Fig. 3f) further indicated that Ni/Cu-MOFs (7:1) film was formed by tiny sheet structures. In addition, it was shown in Mapping images (Fig. S4) that Ni and Cu elements were uniformly distributed in Ni/Cu-MOFs (7:1). The thermal stability of Ni/Cu-MOFs (7:1) was evaluated by the TGA curve (Fig. S5). Ni/Cu-MOFs (7:1) was thermally decomposed at about 270 °C, which was slightly lower than the decomposition temperature of Ni-MOFs (304 °C) but higher than that of Cu-MOFs (235 °C), This difference may be due to the synergistic effect of bimetal within Ni/Cu-MOFs (7:1) caused by their higher chemical activity (Lou et al., 2018).

The XPS spectra (Fig. S6a) of Ni/Cu-MOFs prepared with different feeding metal molar ratios showed that the binding energy peaks of Ni/Cu-MOFs (1:7), Ni/Cu-MOFs (1:1) and Ni/Cu-MOFs (7:1) were relatively consistent, and the characteristic peaks of Ni 2p and Cu 2p were all found, indicating that Ni/Cu-MOFs could be synthesized under the three kinds of molar ratios. However, the peaks of Cu 2p did not appear in the XPS of Ni/Cu-MOFs (20:1) and Ni/Cu-MOFs (30:1). This result was because that when the content of Ni ions added was much more than that of Cu ions, a large amount of Ni ions occupied the coordination sites, which made it difficult for a smaller amount of Cu ions to participate in the coordination reaction and to synthesize bimetallic MOFs. XPS ratios data of main elements in Ni/Cu-MOFs prepared with different feeding molar ratios (Ni:Cu = 1:7, 1:1, 7:1, 20:1 and 30:1) were presented in the Table S1. It was found that the content of C, N and O elements in MOFs synthesized with different metal molar ratios was not much different. In addition, for MOFs with a ratio of 1:1, 7:1, 20:1 and 30:1, the real metal molar ratios of Ni and Cu were relatively close to the feeding molar ratios. However, for the MOFs with a ratio of 1:7, the difference between the real and the feeding molar ratio was relatively large. This was mainly due to the large amount of Cu ions involved in the coordination to produces MOFs which was easy to precipitate, so the proportion of Cu in the bimetallic MOFs films was relatively small. In addition, the contents of Ni ions and Cu ions in Ni/Cu-MOFs prepared with different feeding molar ratios were determined by ICP-MS (Table S2), suggesting that the final Ni/Cu molar ratios were 1:8.31, 0.83:1, 5.48:1, 17.53:1 and 26.56:1 respectively, close to the feeding molar ratios. The XRD spectra of Ni/Cu-MOFs prepared with different metal molar ratios were shown in Fig. S6b. They all had peaks at 2θ = 7.5° and 33.3° belonging to the characteristic diffraction peaks of Ni-MOFs rather than that of Cu-MOFs, which revealed that Ni ions of the five metal molar ratios could participate in the coordination to form Ni-MOFs. In addition, as the metal molar ratios changed from 1:7 to 30:1, the position of the diffraction peaks ascribed to the (001) crystal plane gradually shifted from 27.7° to 26.9°, indicating an increase of interplanar spacing in the Ni/Cu-MOFs. This was because that the proportion of Ni ions within the formed bimetallic MOFs increased, and the radius of Ni ions was larger than that of Cu ions. The morphologies of Ni/Cu-MOFs films with different molar ratios were shown in Fig. S7. The morphologies of Ni/Cu-MOFs (1:7) and Ni/Cu-MOFs (1:1) were similar to that of monometallic Cu-MOFs. However, it was difficult to form dense MOFs films when the molar amount of Cu ions added was large, which was because that the products formed by the coordination between Cu and HITP tended to aggregate and precipitate. The thin films of Ni/Cu-MOFs (20:1) and Ni/Cu-MOFs (30:1) both exhibited sheet-like stacked morphological structures similar to that of Ni-MOFs.

3.2. Electrical performance

As shown in Fig. S8, the current value of Ni/Cu-MOFs (10:1)-FET tested under the same conditions was reduced compared with that of Ni/Cu-MOFs (7:1)-FET, indicating that the content ratio of Ni ions and Cu ions had an effect on the performance of bimetallic MOFs. The field-effect electrical performances of Ni-MOFs-FET, Cu-MOFs-FET, Ni/Cu-MOFs (7:1)-FET and GOD-GA-Ni/Cu-MOFs (7: 1)-FET tested as liquid-gated devices were shown in Fig. S9. The performance of Cu-MOFs-FET was the worst and its I_{ds}-V_{ds} curve that did not pass the origin indicated a serious leakage current phenomenon, which was because that Cu-MOFs tended to aggregate during the coordination reaction and did not form a good film. The I_{ds}-V_{ds} curve of Ni/Cu-MOFs (7:1)-FET showed good ohmic characteristics and a better linear relationship than those of Ni-MOFs-FET and Cu-MOFs-FET. The current value of Ni/Cu-MOFs (7:1)-FET was increased by an order of magnitude, indicating its more excellent conductivity. This was attributed to the synergistic effect of Ni and Cu in Ni/Cu-MOFs (7:1), enhancing the carriers transfer and increasing the abundant active metal sites, which improved the reactivity of bimetallic MOFs. The I_{ds}-V_{gs} curve of Ni/Cu-MOFs (7:1)-FET revealed that it still possessed bipolar characteristics similar to that of Ni-MOFs (7:1)-FET. Therefore, the conductivity of Ni/Cu-MOFs (7:1)-FET could be affected by the carriers (holes or electrons) accumulated in the MOFs channel layers, resulting in p-type or n-type doping effects (Kwak et al., 2012). Especially, the current value of the I_{ds}-V_{gs} curve of Ni/Cu-MOFs (7:1)-FET increased, and its extreme point shifted slightly to the negative direction compared with that of the Ni-MOFs-FET, which was due to the n-type doping effect caused by the strong electronegativity of Cu ions (Kim et al., 2017). The current value of GOD-GA-Ni/Cu-MOFs (7:1)-FET was lower than that of untreated Ni/Cu-MOFs (7:1)-FET but higher than that of Ni-MOFs-FET. This was because the modification of glucose enzyme made a certain interference on the carrier transfer (Hudak and Barton, 2005). Moreover, the extreme points at the I_{ds}-V_{gs} curve of GOD-GA-Ni/Cu-MOFs (7:1)-FET shifted significantly toward the negative direction. This was because when Ni/Cu-MOFs were modified with negatively charged GOD in the PBS solution via GA, it was quite equivalent to introducing negative charges in Ni/Cu-MOFs to enhance their n-type doping effect (De La Garza et al., 2003). The maximum transconductance (g_m) of the GOD-GA-Ni/Cu-MOFs (7:1)-FET was 20.47 μS (Fig. S10), and the carrier mobility (μ) of it as a liquid-gated device was calculated to be 401.05 $cm^2\ V^{-1}s^{-1}$ according to Formula S1. The current switching ratio (I_{on}/I_{off}) was 4.89 and the threshold voltage (V_{th}) was 0.32 V.

3.3. Glucose detection

The electrical property of the GOD-GA-Ni/Cu-MOFs (7:1)-FET in PBS solutions of different pH were shown in Fig. S11, and its conductance was calculated according to the I-V_{ds} curve. It could be found that as the pH increased from 5.8 to 8, the conductivity of the device improved. However, due to the poor acid-based resistance of MOFs and the pH range of actual blood glucose (pH = 7.35–7.45), a pH of 7.4 was chosen as the detection environment to study the glucose detection of the GOD-GA-Ni/Cu-MOFs (7:1)-FET. The glucose concentration test result of the GOD-GA-Ni/Cu-MOFs (7:1)-FET was shown in Fig. 4a. The glucose sensor responded instantly and generated current signal when the glucose was added to the liquid cell. And the respond time did not exceed 5 s (the insert of Fig. 4a), which indicated that the GOD-GA-Ni/Cu-MOFs (7:1)-FET had a fast response to glucose detection. As the glucose concentration gradually increased from 1 μM to 50 mM, the source-drain current of the FET showed a step change, and its absolute value decreased, which was due to the enzymatic reaction between glucose and GOD temporarily changing the protonation state of conductive MOFs. (Ahmad et al., 2015; Liu et al., 2018). The enzymatic reaction of glucose was as follows:

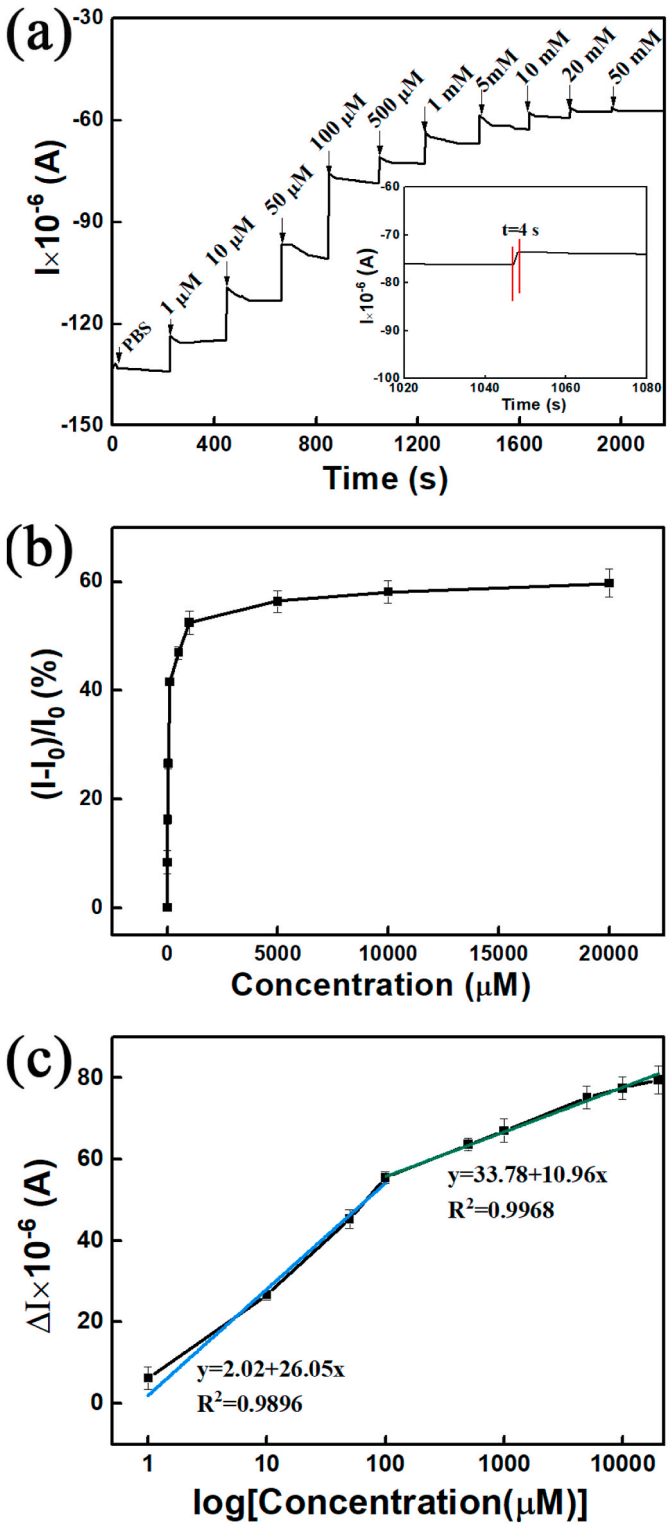

Fig. 4. (a) Glucose concentration test curve of GOD-GA-Ni/Cu-MOFs (7:1)-FET in the range of 1 μM–50 mM with the fixed V_{gs} = −0.1 V and V_{ds} = −0.1 V. In the inset is the data of 100 μM Glucose detected by GOD-GA-Ni/Cu-MOFs (7:1)-FET. (b) Relationship curve between the change of current value ($(I–I_0)/I_0$) and the glucose concentration. (c) Relationship curve between the change in current and the logarithmic value of glucose concentration (the black curve), and its linear fitting curves (the blue one and the green one). The fitting linear relationship was y = 2.02 + 26.05x in the range of 1–100 μM, and was y = 33.78 + 10.96x in the range of 100 μM–20 mM. (For interpretation of the references to color in this figure legend, the reader is referred to the Web version of this article.)

$$D-glucose + H_2O + O_2 \xrightarrow{GOD} gluconolactone + H_2O_2 \quad (1)$$

$$H_2O_2 \rightarrow O_2 + 2H^+ + 2e^- \quad (2)$$

Glucose was converted to gluconolactone and hydrogen peroxide (H_2O_2) Under the catalysis of GOD according to the reaction (1). Then, H_2O_2 dissociated further and generated hydrogen ions (H^+) and electrons (e^-) under the gate voltage with the reaction (2). Because the connection effect of GA enabled GOD closer to the surface of Ni/Cu-MOFs, the H^+ generated by the enzyme reaction gradually increased and accumulated on the interface between the MOFs channel layers and the solution, making an inducing effect on the channel layers (Kwak et al., 2012). Ni/Cu-MOFs behaved as a p-type semiconductor at the gate voltage (−0.1 V). Therefore, under the induction of H^+, the number of main carriers (holes) in the Ni/Cu-MOFs channel layer reduced, resulting in a decrease in conductance and a change on current value of the FET with the increase of glucose from low concentrations to high concentrations (Ahmad et al., 2015; Shan et al., 2018). By testing the solution containing only PBS, the influence of PBS on the test current signal was eliminated (Fig. S12a). In addition, the glucose concentration tests of GOD-GA-Ni-MOFs-FET, GA-Ni/Cu-MOFs (7:1)-FET and Ni/Cu-MOFs (7:1)-FET were conducted to serve as control experiments. The GOD-GA-Ni-MOFs (7:1)-FET showed a certain current change with glucose concentration increasing but not a continuous step change (Fig. S12b), indicating its undesirable detection to glucose. The test results of GA-Ni/Cu-MOFs (7:1)-FET (Fig. S12c) and Ni/Cu-MOFs (7:1)-FET (Fig. S12d) showed their poor response to glucose, which further proved that the current change of the device was mainly caused by the enzymatic reaction of glucose. The morphology (Fig. S13) of GOD-GA-Ni/Cu-MOFs (7:1) after glucose concentration test indicated that the solution test environment had little damage to the structure of the MOFs films. Moreover, the glucose concentration test of the BSA-GOD-GA-Ni/Cu-MOFs (7:1)-FET was conducted to explore the effect of non-specific adsorption. The current change of BSA-GOD-GA-Ni/Cu-MOFs (7:1)-FET in glucose detection was smaller than that of GOD-GA-Ni/Cu-MOFs (7:1)-FET (Figs. S14a and b). Part of the reason might be due to the existence of non-characteristic adsorption, and the other part was because of the reduced conductivity of the device modified with BSA (as shown in Figs. S14c and d).

The relationship curve between the change of current value ($\triangle I = I–I_0$) and the glucose concentration was shown in Fig. 4b. It could be seen that the current began to decrease and became gentle when the glucose concentration reached to 20 mM, while when the concentration continuously increased to 50 mM, the current hardly changed. This may be due to the limited number of enzymes modified on the enzyme sensor making the detection of glucose to reach saturation (Makaram et al., 2014). The good detection of GOD-GA-Ni/Cu-MOFs (7:1)-FET in a wide concentration range of glucose (1 μM–20 mM) was because of the high surface area ratio and abundant electroactive sites of bimetallic MOFs, making it have better adsorption and larger reaction surface area for glucose molecules. The relationship curve between the change in current and the logarithmic value of glucose concentration (the black curve), and its linear fitting curves (the blue one and the green one) were presented in Fig. 4c. The device showed good linear relationships in the both glucose concentration range of 1–100 μM and 100 μM–20 mM, respectively. The fitting linear relationship was y = 2.02 + 26.05x in the low concentration range of 1–100 μM, and was y = 33.78 + 10.96x in the high range of 100 μM–20 mM. And the linear correlation coefficients (R^2) were 0.9896 and 0.9968, respectively. The sensitivity of the FET sensor was calculated by the slope of each linear range to be 26.05 $\mu Acm^{-2}mM^{-1}$ in the 1–100 μM of glucose, and to be 10.96 $\mu Acm^{-2}mM^{-1}$ in the 100 μM–20 mM of glucose. According to the Formula S2, the lower limit of detection (LOD) was estimated to be 0.51 μM. The comparation of performance between the GOD-GA-Ni/Cu-MOFs (7:1)-FET and other previously reported FET-based glucose sensors was shown in Table 1. It could be seen that

Table 1
Comparison of performances between the GOD-GA-Ni/Cu-MOFs (7:1)-FET and other FET-based glucose sensors.

Method	Detection Limit (μM)	Linear Range (mM)	Sensitivity ($\mu Acm^{-2}mM^{-1}$)	Ref
Fe_2O_3–ZnO-FET	12	0.05–18	105.75	Ahmad et al. (2017)
Nafion/GOx/Zn-FET	70	0.0–80	22.3	Bhat et al. (2017)
GOx-ZnO NRs-FET	0.07	0.05–70	32.27	Ahmad et al. (2015)
GOx-silk-graphene-FET	100	0.1–10	2.5	You and Pak (2014)
GOx/ZnO NWs-FET	50	0.2–2	19.5	Pradhan et al. (2010)
GOx-PMMA/graphene-FET	3.3	3.3–10.9	/	Kwak et al. (2012)
GOD-GA-Ni/Cu-MOFs-FET	0.51	0.001–20	26.05/10.96	This work

the GOD-GA-Ni/Cu-MOFs (7:1)-FET, as a novel glucose sensor, had higher sensitivity, a wider detection range and a lower detection limit. Moreover, the glucose concentration test results of three GOD-GA-Ni/Cu-MOFs (7:1)-FET showed a low standard deviation (RSD) of 3.32% (Fig. S15), indicating that the sensor has good reliability for glucose detection.

Sucrose, fructose, UA, AA, galactose and lactose were used as interferences to test the specificity of GOD-GA-Ni/Cu-MOFs (7:1)-FET for glucose detection (Fig. 5a and Fig. S16). The current of the sensor decreased significantly when glucose was added first. Then, the current did not change when other interfering substances were added sequentially, but changed again after the glucose was added again. The phenomenon showed that the prepared GOD-GA-Ni/Cu-MOFs (7:1)-FET could achieve the specific detection to glucose. The stability of GOD-GA-Ni/Cu-MOFs (7:1)-FET was evaluated by measuring its current response to glucose in a concentration range (1–500 μM) every two days within a week (Fig. 5b). The current signal dropped slightly by 2.12% on the second day, and then decreased by 16.72% and 20.60% on the fourth and sixth days, respectively (Fig. 5c). In order to further explore the lifetime of the sensor, the concentration tests of four GOD-GA-Ni/Cu-MOFs (7:1)-FETs after being placed for 0, 1, 2 and 3 weeks respectively were conducted (as shown in Fig. S17). It was found that as the storage time was longer, the current signal of the sensor decayed more. And the current of the sensor placed for three weeks was significantly reduced and its response to glucose became weaker. The decrease of the current response may be due to the inactivation of the modified GOD and the loss of the enzyme during the washing process. Therefore, the GOD-GA-Ni/Cu-MOFs (7:1)-FET enzyme sensor could be used as a disposable biosensor.

4. Conclusion

In conclusion, a glucose sensor (GOD-GA-Ni/Cu-MOFs-FET) with bimetallic MOFs as channel layers was prepared via a simple *in situ* method. The prepared sensor had good field effect performance when the feeding molar ratio of Ni ions and Cu ions was 7: 1, and showed excellent responds to glucose with a wide concentration range of 1 μM–20 mM, a higher sensitivity of 26.05 $\mu Acm^{-2}mM^{-1}$, and a low detection limit of 0.51 μM. This was mainly due to the synergistic effect of Ni ions and Cu ions within bimetallic MOFs and the modification of GA. Although the GOD-GA-Ni/Cu-MOFs-FET did not have good long-term stability, it could be used as a disposable and real time glucose sensor because of its good specificity, reproducibility and fast respond time. Therefore, this work can pave the way for the future research on FET-type biosensors based on bimetallic MOFs.

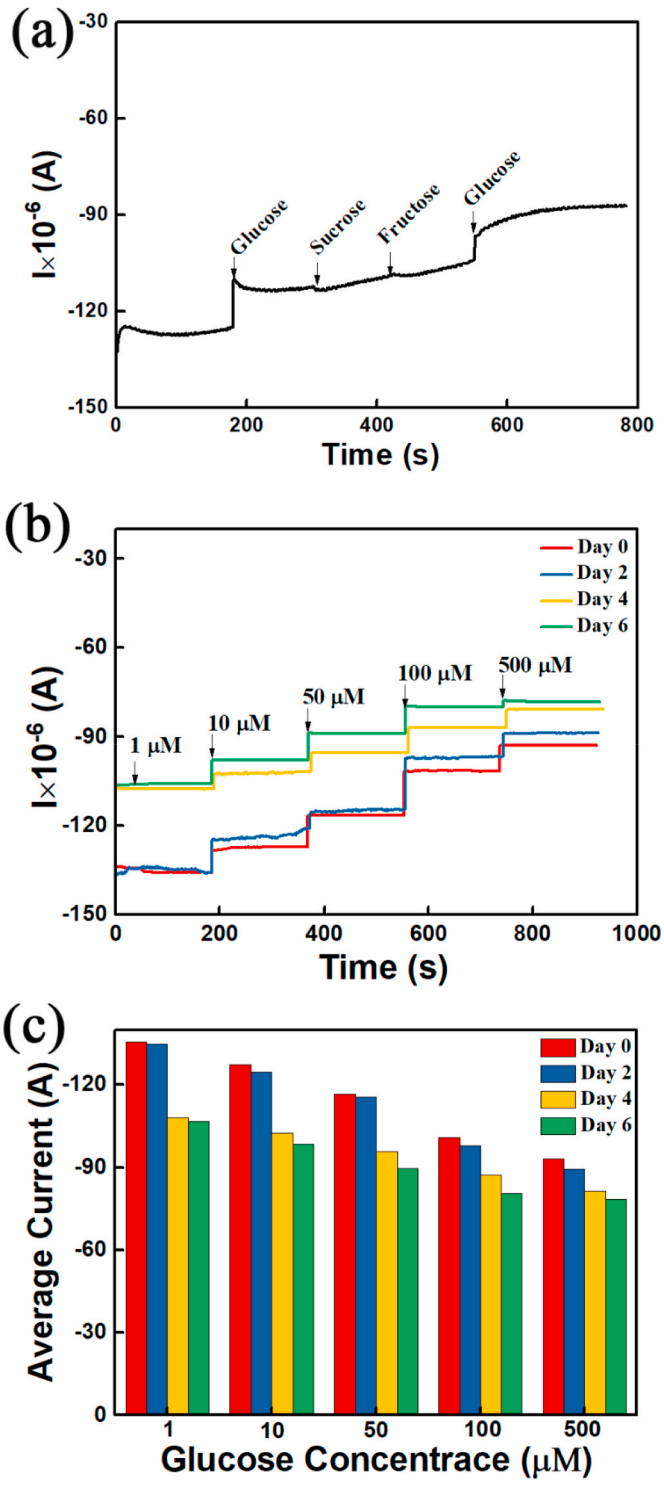

Fig. 5. (a) Specificity test of the GOD-GA-Ni/Cu-MOFs (7:1)-FET when 5 μL of 100 μM glucose, sucrose and fructose were added in sequence. (b) Stability test of the GOD-GA-Ni/Cu-MOFs (7:1)-FET placed under constant temperature and humidity conditions for a week, and its glucose detection performance was tested every two days in a week. (c) Glucose current response loss of GOD-GA-Ni/Cu-MOFs (7:1)-FET sensor at the 0, 2nd, 4th, and 6th day.

CRediT authorship contribution statement

Bingfang Wang: Methodology, Formal analysis, Writing - original draft, Writing - review & editing. **Yuanyuan Luo:** Project administration, Writing - review & editing. **Lei Gao:** Formal analysis, Resources. **Bo**

Liu: Data curation. **Guotao Duan:** Conceptualization, Supervision, Funding acquisition.

Declaration of competing interest

The authors declare that they have no known competing financial interests or personal relationships that could have appeared to influence the work reported in this paper.

Acknowledgments

The authors acknowledge the financial supports from National Key R&D Program of China (2019YFB2006002), National Natural Science Foundation of China (Grant No. 11674320) and Key Research Projects of the Frontier Science CAS (QYZDB-SSW-JSC017).

Appendix A. Supplementary data

Supplementary data to this article can be found online at https://doi.org/10.1016/j.bios.2020.112736.

References

Abuzalat, O., Wong, D., Park, S.S., Kim, S., 2020. Nanoscale 12, 13523–13530. https://doi.org/10.1039/d0nr01653e.
Ahmad, R., Ahn, M.S., Hahn, Y.B., 2017. Electrochem. Commun. 77, 107–111. https://doi.org/10.1016/j.elecom.2017.03.006.
Ahmad, R., Tripathy, N., Park, J.H., Hahn, Y.B., 2015. Chem. Commun. 51, 11968–11971. https://doi.org/10.1039/c5cc03656a.
Bhat, K.S., Ahmad, R., Yoo, J., Hahn, Y., 2017. J. Colloid Interface Sci. 506, 188–196. https://doi.org/10.1016/j.jcis.2017.07.037.
Campbell, M.G., Sheberla, D., Liu, S.F., Swager, T.M., Dincə, M., 2015. Angew. Chem. Int. Ed. 54, 4349–4352. https://doi.org/10.1002/anie.201411854.
Cao, C., Ma, D.D., Xu, Q., Wu, X.T., Zhu, Q.L., 2019. S Adv. Funct. Mater. 29, 1–8. https://doi.org/10.1002/adfm.201807418.
Chen, H., Li, L., Guo, H., Wang, X., Qin, W., 2015. RSC Adv. 5, 13805–13808. https://doi.org/10.1039/c4ra15037f.
Chen, J., Xu, Q., Shu, Y., Hu, X., 2018. Talanta 184, 136–142. https://doi.org/10.1016/j.talanta.2018.02.057.
Colmegna, P.H., Sanchez-Pena, R.S., Gondhalekar, R., Dassau, E., Doyle, F.J., 2016. IEEE Trans. Biomed. Eng. 63, 1192–1200. https://doi.org/10.1109/TBME.2015.2487043.
De La Garza, L., Jeong, G., Liddell, P.A., Sotomura, T., Moore, T.A., Moore, A.L., Gust, D., 2003. J. Phys. Chem. B 107, 10252–10260. https://doi.org/10.1021/jp030360j.
Depciuch, J., Stanek-Widera, A., Warchulska, M., Lange, D., Sarwa, K., Koziorowska, A., Kula, M., Cebulski, J., 2019. Infrared Phys. Technol. 102, 102989. https://doi.org/10.1016/j.infrared.2019.102989.
Dhanjai Lu, X., Wu, L., Chen, J., Lu, Y., 2020. Anal. Chem. 92, 5830–5837. https://doi.org/10.1021/acs.analchem.9b05466.
Fang, G., Wang, Q., Zhou, J., Lei, Y., Chen, Z., Wang, Z., Pan, A., Liang, S., 2019. ACS Nano 13, 5635–5645. https://doi.org/10.1021/acsnano.9b00816.
Guo, C., Su, F., Song, Y., Hu, B., Wang, M., He, L., Peng, D., Zhang, Z., 2017a. ACS Appl. Mater. Interfaces 9, 41188–41199. https://doi.org/10.1021/acsami.7b14952.
Guo, W., Xia, W., Cai, K., Wu, Y., Qiu, B., Liang, Z., Qu, C., Zou, R., 2017b. Small 13, 1702049. https://doi.org/10.1002/smll.201702049.
Heidari, H., Habibi, E., 2016. Microchim. Acta. 183, 2259–2266. https://doi.org/10.1007/s00604-016-1862-z.
Hudak, Nicholas S., Barton, Scott Calabrese, 2005. Mediated biocatalytic cathode for direct methanol membrane-electrode assemblies. J. Electrochem. Soc. 152, A876–A881. https://doi.org/10.1149/1.1887146.
Kim, D.M., Moon, J.M., Lee, W.C., Yoon, J.H., Choi, C.S., Shim, Y.B., 2017. Biosens. Bioelectron. 91, 276–283. https://doi.org/10.1016/j.bios.2016.12.046.
King, H., Aubert, R.E., Herman, W.H., 1998. Diabetes Care 21, 1414–1431. https://doi.org/10.2337/diacare.21.9.1414.
Kou, X., Tong, L., Shen, Y., Zhu, W., Yin, L., Huang, S., Zhu, F., Chen, G., Ouyang, G., 2020. Biosens. Bioelectron. 156, 112095. https://doi.org/10.1016/j.bios.2020.112095.
Kwak, Y.H., Choi, D.S., Kim, Y.N., Kim, H., Yoon, D.H., Ahn, S.S., Yang, J.W., Yang, W.S., Seo, S., 2012. Biosens. Bioelectron. 37, 82–87. https://doi.org/10.1016/j.bios.2012.04.042.
Li, J., Hu, H., Li, H., Yao, C., 2017. J. Mater. Sci. 52, 10455–10469. https://doi.org/10.1007/s10853-017-1221-4.
Li, Jiantang, Bhatt, P.M., Li, Jiyang, Eddaoudi, M., Liu, Y., 2020. Adv. Mater. 2002563. https://doi.org/10.1002/adma.202002563.
Liao, X., Fu, H., Yan, T., Lei, J., 2019. Biosens. Bioelectron. 146, 111743. https://doi.org/10.1016/j.bios.2019.111743.
Liu, A., Lang, Q., Liang, B., Shi, J., 2017. Biosens. Bioelectron. 87, 25–30. https://doi.org/10.1016/j.bios.2016.07.050.
Liu, Q., Liu, Y., Wu, F., Cao, X., Li, Z., Alharbi, M., Abbas, A.N., Amer, M.R., Zhou, C., 2018. ACS Nano 12, 1170–1178. https://doi.org/10.1021/acsnano.7b06823.
Lou, X., Ning, Y., Li, C., Hu, X., Shen, M., Hu, B., 2018. Sci. China Mater. 61, 1040–1048. https://doi.org/10.1007/s40843-017-9200-5.
Luo, X., Xia, J., Jiang, X., Yang, M., Liu, S., 2019. Anal. Chem. 91, 15461–15468. https://doi.org/10.1021/acs.analchem.9b03180.
Makaram, P., Owens, D., Aceros, J., 2014. Diagnostics 4, 27–46. https://doi.org/10.3390/diagnostics4020027.
Piao, Y., Han, D.J., Azad, M.R., Park, M., Seo, T.S., 2015. Biosens. Bioelectron. 65, 220–225. https://doi.org/10.1016/j.bios.2014.10.032.
Pradhan, D., Niroui, F., Leung, K.T., 2010. ACS Appl. Mater. Interfaces 2, 2409–2412. https://doi.org/10.1021/am100413u.
Rahman, M.M., Ahammad, A.J.S., Jin, J.H., Ahn, S.J., Lee, J.J., 2010. Sensors 10, 4855–4886. https://doi.org/10.3390/s100504855.
Roda, A., Arduini, F., Mirasoli, M., Zangheri, M., Fabiani, L., Colozza, N., Marchegiani, E., Simoni, P., Moscone, D., 2020. Biosens. Bioelectron. 155, 112093. https://doi.org/10.1016/j.bios.2020.112093.
Shan, J., Li, J., Chu, X., Xu, M., Jin, F., Wang, Xiaojun, Ma, L., Fang, X., Wei, Z., Wang, Xiaohua, 2018. RSC Adv. 8, 7942–7948. https://doi.org/10.1039/c7ra13614e.
Sheberla, D., Sun, L., Blood-Forsythe, M.A., Er, S., Wade, C.R., Brozek, C.K., Aspuru-Guzik, A., Dincă, M., 2014. J. Am. Chem. Soc. 136, 8859–8862. https://doi.org/10.1021/ja502765n.
Shen, J.Q., Liao, P.Q., Zhou, D.D., He, C.T., Wu, J.X., Zhang, W.X., Zhang, J.P., Chen, X. M., 2017. J. Am. Chem. Soc. 139, 1778–1781. https://doi.org/10.1021/jacs.6b12353.
Song, Y., Shan, B., Feng, B., Xu, P., Zeng, Q., Su, D., 2018. RSC Adv. 8, 27008–27015. https://doi.org/10.1039/C8RA04596H.
Su, Y., Yu, J., Li, Y., Phua, S.F.Z., Liu, G., Lim, W.Q., Yang, X., Ganguly, R., Dang, C., Yang, C., Zhao, Y., 2018. Chem. Commun. 1, 12. https://doi.org/10.1038/s42004-018-0016-0.
Vikas Yadav, M.K., Kumar, P., Verma, R.K., 2020. Food Chem. 332, 127346. https://doi.org/10.1016/j.foodchem.2020.127346.
Wang, H.C., Lee, A.R., 2015. J. Food Drug Anal. 23, 191–200. https://doi.org/10.1016/j.jfda.2014.12.001.
Wang, J., 2008. Chem. Rev. 108, 814–825. https://doi.org/10.1021/cr068123a.
Wei, X., Hu, W., Peng, H., Xiong, Y., Xiao, P., Zhang, Y., Cao, G., 2019. Small 15, 1902280. https://doi.org/10.1002/smll.201902280.
Yadav, J., Rani, A., Singh, V., Murari, B.M., 2015. Biomed. Signal Process Contr. 18, 214–227. https://doi.org/10.1016/j.bspc.2015.01.005.
Yang, J., Yang, Y.W., 2020. Small 16, 1906846. https://doi.org/10.1002/smll.201906846.
You, X., Pak, J.J., 2014. Sensor. Actuator. B Chem. 202, 1357–1365. https://doi.org/10.1016/j.snb.2014.04.079.
Zhang, D., Wang, Z., Li, J., Hu, C., Zhang, X., Jiang, B., Cao, Z., Zhang, J., Zhang, R., 2020. RSC Adv. 10, 9063–9069. https://doi.org/10.1039/c9ra08723k.
Zhao, X., Pattengale, B., Fan, D., Zou, Z., Zhao, Y., Du, J., Huang, J., Xu, C., 2018. ACS Energy Lett. 3, 2520–2526. https://doi.org/10.1021/acsenergylett.8b01540.
Zhou, H., Zheng, M., Tang, H., Xu, B., Tang, Y., Pang, H., 2020. Amorphous intermediate derivative from ZIF-67 and its outstanding electrocatalytic activity. Small 16, 1904252. https://doi.org/10.1002/smll.201904252.
Zhou, W., Huang, D.D., Wu, Y.P., Zhao, J., Wu, T., Zhang, J., Li, D.S., Sun, C., Feng, P., Bu, X., 2019. Angew. Chem. Int. Ed. 58, 4227–4231. https://doi.org/10.1002/anie.201813634.
Zhu, X., Yuan, S., Ju, Y., Yang, J., Zhao, C., Liu, H., 2019. Anal. Chem. 91, 10764–10771. https://doi.org/10.1021/acs.analchem.9b02328.
Zuo, Y., Chen, L., Hu, X., Wang, F., Yang, Y., 2020. Micromachines 11, 383–397. https://doi.org/10.3390/MI11040383.